General Disclaimer

One or more of the Following Statements may affect this Document

- This document has been reproduced from the best copy furnished by the organizational source. It is being released in the interest of making available as much information as possible.

- This document may contain data, which exceeds the sheet parameters. It was furnished in this condition by the organizational source and is the best copy available.

- This document may contain tone-on-tone or color graphs, charts and/or pictures, which have been reproduced in black and white.

- This document is paginated as submitted by the original source.

- Portions of this document are not fully legible due to the historical nature of some of the material. However, it is the best reproduction available from the original submission.

Kenneth J. Baumeister
Lewis Research Center
Cleveland, Ohio

and

Scott J. Horowitz
Lockheed-Georgia
Marietta, Georgia

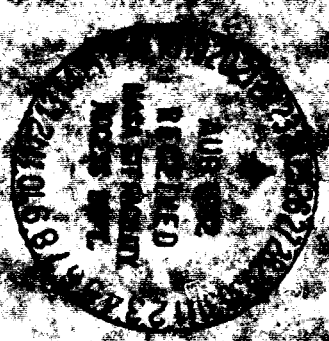

Prepared for the
1980 Winter Annual Meeting of the
American Society of Mechanical Engineers
Phoenix, Arizona, November 14–19, 1980

NASA

FINITE ELEMENT-INTEGRAL SIMULATION OF STATIC AND FLIGHT FAN NOISE RADIATION FROM THE JT15D TURBOFAN ENGINE

Kenneth J. Baumeister
National Aeronautics and Space Administration
Lewis Research Center
Cleveland, Ohio 44135

and

Scott J. Horowitz
Lockheed-Georgia
Marietta, Georgia

E-1232

ABSTRACT

An iterative finite element-integral technique is used to predict the sound field radiated from the JT15D turbofan inlet. The sound field is divided into two regions: the sound field within and near the inlet which is computed using the finite element method and the radiation field beyond the inlet which is calculated using an integral solution technique. The velocity potential formulation of the acoustic wave equation was employed in the program. For some single mode JT15D data, the theory and experiment are in good agreement for the far field radiation pattern as well as suppressor attenuation. Also, the computer program is used to simulate flight effects that cannot be performed on a ground static test stand.

NOMENCLATURE

A	area
$A_{1,2,..}$	flow coefficients
C	velocity of sound normalized to the stagnation speed of sound C_0
C_0	stagnation speed of sound
d_0	internal duct diameter (normalized by d_0 to a dimensionless value of unity)
E	total number of elements
e	element number
F	function equation, see Eq. (4)
f	initial condition function, see Eq. (14)
g	surface potential in far field, Eq. (16)
i	$\sqrt{-1}$
k	wave number
M	total number of unknowns
M_0	Mach number
m	spinning mode number, see Eq. (3)
N	finite element weighting function
n	node number
p	pressure normalized by $\rho_0 C_0^2$
R	far field position (distance from exit plane centerline) normalized by d_0
r	radial coordinate normalized by duct diameter d_0
r_0	$d_0/2$
t	time normalized by d_0/C_0
Z	impedance
Z_i	exit impedance internal region
Z_e	exit impedance external region
z	axial coordinate
γ	specific heat ratio
θ	angular coordinate
ρ	density normalized by ρ_0
ρ_0	stagnation density
Φ	general flow potential normalized by $C_0 d_0$
ϕ	acoustic flow potential
$\bar{\Phi}$	mean flow potential
ω	angular frequency normalized by C_0/d_0

Superscripts

-	mean value

e element number

* transformed value

Subscripts

i,j,k,l index number

I iteration index

n normal

s surface

INTRODUCTION

For over a decade, the generation, suppression, and propagation of noise in turbofan engines has been investigated at the NASA Lewis Research Center. From the standpoint of design and capital costs, as well as operational manpower, test facilities are expensive to operate. To help reduce future costs, both in-house and contractual efforts have been used to develop finite difference and finite element programs to simulate sound propagation in turbofan engines. References (1) and (2) contain a literature review of the techniques, advantages, and limitations associated with the various numerical solutions of the sound propagation equations in ducts. The purpose of the present paper is to investigate how accurately a newly developed hybrid finite element-integral program (3) simulates the measured noise radiated from the JT15D inlet.

The velocity potential formulation of the acoustic wave equation was employed in the finite element-integral program presented herein, since it reduced the computer storage and running time by an order of magnitude compared to the more general linearized gas dynamics formulation. On the other hand, when rotational flow exists in the inlet (wall and center body boundary layers), the potential flow cannot be used to estimate the effects of shear (4). However, since the flow into an inlet is reasonably modeled by potential flow and since boundary layers are small, the acoustic velocity potential is ideally suited for acoustic inlet calculations.

The turbomachinery noise produced within the engine propagates down the inlet duct (also the exit) and radiates to the surrounding environment. One major problem in numerical simulation of the inlet is what boundary condition to use at the exit of the duct (1, p. 273, or 5). To overcome this problem, the present analysis separates the acoustic field into two regions: the "interior" region within the inlet and in the vicinity of the inlet lip, and the exterior region consisting of the unbounded region surrounding the inlet. The interior region contains multidimensional flow while the exterior region is assumed to contain only uniform flow. In this hybrid method, a finite element program is used to solve for the interior acoustic field, while an integral technique (6) is employed in the far field. Numerical iteration between the interior and exterior regions is required to obtain a continuous acoustic field across the interface.

For comparison between experiment and theory, the inlet data from acoustic treatment experiments with a JT15D engine were chosen. In the special JT15D experiment, documented in Ref. (7), one acoustic mode was made to dominate the noise spectrum. Thus, the usual problems of noise floors and separation of acoustic modes were to a large extent eliminated in the data reduction. The results of the present paper will include the effects of the center body, inlet lip shape, and flow gradients on the far field radiation pattern and the attenuation of suppressors used in the JT15D experiments of Ref. (7).

Finally, for a static engine or fan test rig, one major limitation is the inability to simulate the effects of flight on the flow characteristics in the inlet and one the fan source noise and its radiation. A secondary purpose of this paper was to determine the changes in the acoustic radiation due to flow entering the inlet as seen by an engine in flight.

STATIC TEST DATA

As described in the Introduction, theoretical comparisons will be made with the previously published inlet acoustic data for the JT15D engine (7). The acoustic tests outlined in Ref. (7) were performed at the NASA Lewis Vertical Lift Facility. A photograph of the JT15D engine mounted on the test stand is shown in Fig. 1. The spherical inflow control screen covering the inlet was used to reduce turbulence and distortion in the inlet flow. The engine exhaust was connected to a large muffler to suppress aft fan and jet noise. The engine was mounted 2.9 m or 5.4 fan diameters above the concrete pad to minimize ground plane effects on the inlet flow.

The JT15D engine is a two-spool turbofan engine with a nominal 3.3 bypass ratio and a rated thrust of 9790 N. The fan is 53.5 cm in diameter and has 28 blades with 66 exit guide vanes. The blade to vane number ratio for this fan results in a cutoff fundamental rotor-stator interaction tone. The inlet used with this engine is shown in Fig. 2. This inlet has a constant 53.3 cm internal diameter and is fitted to a bellmouth which in turn is attached to a large constant diameter nacelle.

A spool piece with 41 equally spaced radial rods was attached to the engine front flange, as shown in Fig. 2. The wakes of these rods interact with the 28 fan blades to produce a BPF tone with 13 circumferential lobes. At fan speeds between 6400 and 8400 rpm only the lowest order radial mode can propagate, which is ideal for the theoretical comparisons.

Provisions were made for an SDOF (single degree of freedom) acoustic liner to be placed just upstream of the rod section of the inlet (see Fig. 2). This suppressor section was replaceable so that different treatment designs could be tested. The acoustic liners were designed by theory to attenuate the 13 lobe mode produced by the interaction of the inlet rods and the engine fan. Maximum attenuation efficiency was sought for this mode at the blade passage frequency of 3150 Hz with an average duct Mach number of -0.147.

The experimental data will later be presented along with the theoretical results.

MATHEMATICAL FORMULATION

The formulation of the problem first involves specification of the governing equations and boundary conditions. Next, finite element theory will be used to solve for the acoustic parameters within the inlet, while an integral technique will be employed to determine the acoustic parameters outside the engine. Two different mathematical techniques are employed here to overcome the classical closure problem of specifying a nonreflective exit boundary far from the engine. Since a direct extension of the finite element technique into the far field is not possible, the integral technique was used in conjunction with the finite element algorithm. Iteration will be required

to obtain a continuous solution for the acoustic quantities at the interface separating the interior and exterior domains. Each of these topics will now be briefly discussed.

Acoustic Equations

Consider the inlet shown in Fig. 3. The flow of air is assumed to be inviscid, nonheat conducting, and irrotational. Under these assumptions, the flow in the duct can be described in cylindrical coordinates by the flowing nondimensional nonlinear partial differential equation for the flow potential Φ (8):

$$C^2\left\{\Phi_{rr} + \Phi_r/r + \Phi_{\theta\theta}/r^2 + \Phi_{zz}\right\} - \Phi_{tt} = 2\Phi_r\Phi_{tt} + 2\Phi_\theta\Phi_{\theta t}/r^2 + 2\Phi_z\Phi_{zt} + \Phi_r^2\Phi_{rr} + \Phi_\theta^2\Phi_{\theta\theta}/r^4 + \Phi_z^2\Phi_{zz} + 2\Phi_r\Phi_\theta\Phi_{r\theta}/r^2 + 2\Phi_r\Phi_z\Phi_{rz} + 2\Phi_z\Phi_\theta\Phi_{z\theta}/r^2 - \Phi_r\Phi_\theta^2/r^3 \quad (1)$$

with the Z axis coinciding with the turbofan inlet axis and

$$C^2 = 1. - (\gamma - 1)\left[\Phi_t + \frac{1}{2}\left(\Phi_r^2 + \Phi_\theta^2/r^2 + \Phi_z^2\right)\right] \quad (2)$$

where the subscripts indicate partial differentiation with respect to the subscripted variables. These symbols and those following are listed in the nomenclature.

To obtain the acoustic equations for the inlet, first the flow potential Φ is rewritten as the sum of a steady axisymmetric mean flow potential $\bar{\Phi}(r,z)$ and an acoustic potential ϕ

$$\Phi = \bar{\Phi} + \phi(r,z)\, e^{-i(\omega t - m\theta)} \quad (3)$$

To account for spinning modes, the acoustic potential in Eq. (3) has been modified to include $e^{im\theta}$. Also, the solutions have been assumed to be harmonic ($e^{-i\omega t}$) in time.

The mean flow quantities, $\bar{\Phi}$, are independent of time and thereby satisfy the steady mean flow equation. Substituting Eq. (3) into Eq. (1), eliminating the mean flow quantities, and neglecting nonlinear acoustic quantities yields:

$$F(\phi) = A_1\phi_{rr} + A_2\phi_{zz} + A_3\phi_{rz} + A_4\phi_r + A_5\phi_z + A_6\phi = 0 \quad (4)$$

where

$$A_1 = \bar{c}^2 - \bar{\Phi}_r^2 \quad (5)$$

$$A_2 = \bar{c}^2 - \bar{\Phi}_z^2 \quad (6)$$

$$A_3 = -2\bar{\Phi}_r\bar{\Phi}_z \quad (7)$$

$$A_4 = -(\gamma - 1)\,\bar{\Phi}_{rr}\bar{\Phi}_r - 2\,\bar{\Phi}_{rz}\bar{\Phi}_z + \bar{C}^2/r - (\gamma - 1)\,\Phi_r^2/r - (\gamma - 1)\,\bar{\Phi}_r\bar{\Phi}_{zz} - i\,[2\omega\bar{\Phi}_r] \quad (8)$$

$$A_5 = -(\gamma + 1)\,\bar{\Phi}_{zz}\bar{\Phi}_z - 2\,\bar{\Phi}_{rz}\bar{\Phi}_r - (\gamma - 1)\,\bar{\Phi}_{rr}\bar{\Phi}_z - (\gamma - 1)\,\bar{\Phi}_z\bar{\Phi}_r/r - i\,[2\omega\bar{\Phi}_z] \quad (9)$$

$$A_6 = \omega^2 - m^2\bar{c}^2/r^2 - \omega(\gamma - 1)\left(\bar{\Phi}_{rr} + \bar{\Phi}_r/r + \bar{\Phi}_{zz}\right) \quad (10)$$

where the A's contain all the mean flow quantities. The acoustic potential ϕ is complex.

Since the steady flow is assumed to be axisymmetric, the equation expressing conservation of acoustic momentum in the θ direction can be integrated to give the following relationship between the pressure perturbation P and the velocity potential ϕ:

$$p = -\bar{\rho}\,(i\omega\phi + \bar{\Phi}_z\phi_z + \bar{\Phi}_r\phi) \quad (11)$$

Boundary Conditions

To prescribe the boundary conditions, the engine is divided into a finite interior region and an exterior region, as shown in Fig. 3 The rear portion of the inlet is replaced by an ellipsoidal termination since it has been previously established that the geometry of this region has very little effect on the sound radiated from the inlet (6).

Along the axis of symmetry, and the acoustically hard walls (centerbody, part of the duct wall and the nacelle exterior wall) the normal gradient of the acoustic velocity potential is

$$\phi_n = 0 \quad (12)$$

The boundary condition at the surface of a locally reacting sound absorbent soft-wall duct can be expressed in terms of a specific acoustic impedance. Z. Majjigi (9) has shown that a proper formulation of the requirement of continuity of particle displacement yields

$$\phi_n = \frac{-p}{Z} - \frac{1}{i\omega}\,\bar{\Phi}_s\,\frac{\partial}{\partial s}\left(\frac{p}{Z}\right) + \frac{p}{i\omega Z}\,\bar{\Phi}_{nn} \quad (13)$$

where p is given in Eq. (11). In this analysis, it is assumed that the last term in Eq. (13) is negligible since $\bar{\Phi}_{nn}$ is quite small and cannot be accurately calculated by the method currently used for computing the steady flow.

The fan plane is the interface between the inlet and the turbofan engine noise source (rotor and stator blades). Generally, the noise source can be a velocity potential or a pressure source. In the problem considered herein a sound pressure source of the form

$$P(r) = f(r) \quad (14)$$

will be used. As will be shown, a plane radial profile ($f(r)$ = constant) and a Bessel function representation for $f(r)$ will be used. The pressure $P(r)$ is related to $\phi(r)$ through Eq. (11).

Finally, at the interface between the interior and exterior regions an impedance condition

$$Z_{1i} = \frac{-p}{\phi_n} = 1.0 \tag{15}$$

is used to initially close the interior problem. Since the value of Z_{Ii} is not known a priori, an iteration scheme is used to determine the correct value of Z_{Ii}. The subscript I represents an iteration counter, while i stands for interior region. I equals 1 in the first iteration as shown in Eq. (15).

On axis of symmetry in the exterior field, Eq. (12) holds again. Along the interface separating the interior and exterior regions, the potential in the exterior region g(s) must equal the potential in the interior region.

$$g_I(a) = \phi_I(s) \tag{16}$$

and the impedances at the interface must be equal

$$Z_{Ie} = Z_{Ii} \tag{17}$$

Again, ϕ_I and $g_I(s)$ as well as the impedances are not known a priori. The iteration procedure to determine these values will be discussed shortly.

Finally, only outward propagating waves can exist in the far field as the distance from the inlet approaches infinity. By using the free space Green function in the integral solution (6), the absence of reflections in the far field is automatically achieved.

Interior Solution

A finite element method is used to obtain the solutions to Eq. (4) in the interior portion of the inlet. To accomplish this task on the JT15D inlet, the inlet nas been divided into a number of triangular Hermitian elements, as seen in Fig. 4. For clarity, the number of elements shown have been greatly reduced from the actual number used. As shown in Fig. 3, the indices i,j, and k represent the vertices of the triangle and the index ℓ denotes the centroid node. The centroid node is not shown in Fig. 4.

To represent the variation inside the elements of the field variable and its derivatives, the interpolation function for tne Hermitian elements is written as follows

$$\begin{aligned}\phi(r,z) = {} & N_1^e\phi_i + N_2^e\phi_{zi} + N_3^e\phi_{ri} + N_4^e\phi_j + N_5^e\phi_{zj} \\ & + N_6^e\phi_{rj} + N_7^e\phi_k + N_8^e\phi_{zk} + N_9^e\phi_{rk} + N_{10}^e\phi_\ell\end{aligned} \tag{18}$$

where r and z subscripts represent derivatives while the i,j,k,ℓ subscripts represent the node positions. Values of the weighting functions

$N_1^e, N_2^e, \ldots$ are given in Ref. (10).

The unknown nodal values of the velocity potential ϕ and its derivatives are now constrained to satisfy the wave Eq. (4) and the previously discussed boundary conditions by using the Galerkin form of tne method of weighted residuals. For the simpler Lagrange interpolation functions (11) the total number of unknowns would be the total number of vertices and centroids representing the unknown ϕ values at each node. However, using the Hermitian formulation, ϕ, ϕ_r, and ϕ_z are unknowns at each vertex with ϕ only at the centroid. Thus the total number of unknowns M can be expressed as

$$M = 3x \text{ (Number of vertices)} + E \tag{19}$$

where E is the total number of elements each having one centroidal unknown. Obviously, the bandwidth of the solution matrix increases with the Hermitian formulation; however, fewer elements are needed to resolve the pressure field. Also, use of the Hermitian formulation tends to reduce spurious oscillation excited by inaccurate matching at boundaries (12).

Application of the Galerkin finite element method yields the following relationship

$$\sum_{e=1}^{E} \iint_{A_e} N_m^e F(\phi) dA^{(e)} = 0 \tag{20}$$

where $F(\phi)$ represents the wave Eq. (4) and the area of integration is over the element labled e. As given in Eq. (18), N_m^e is the known weighting function for each unknown m associated with a node m of element e. It should be noted that N_m^e is zero for all elements not having the unknown m (ϕ or its derivative) associated with a particular element. For example, vertix node 16 in Fig. 4 will require a summation over only six adjacent elements, while the vertix node 18 along the boundary will require a summation over only three elements. The centroid nodes will require only one integration over only a single element.

When Hermitian elements are used, the analytical integrations of the element equations required by Eq. (20) become formidable. In this case, it is far more practical to evaluate the integrals numerically using a Gauss quadrature scheme. Since the weighting functions are polynomials, the Gauss quadrature is exact (13) and the chance of error is substantially reduced by letting the computer perform the integration.

Equation (20) provided M equations for the M unknown nodal values of ϕ and its derivatives. The remaining task of assembling and solving the matrix equation follows the general approach of finite element methods (3 and 10). In this case, however, the acoustic velocities represented by ϕ_r and ϕ_z are contained in the solution vector and need not be calculated by differentiating the potential.

Exterior Solution

The integral technique is used to solve the wave equation in the far field. In the integral technique, the Green's theorem is used to transform the partial differential equation within a region to an equivalent problem of solving an integral equation over the boundary of the region. For acoustic problems, the integrals vanish at infinity and on the axis of symmetry leaving only the body surface, or in this case the "interface" shown in Fig. 3. The integral technique developed by Meyer et al. (6) will be employed here. It uses a Green's function that satisfies the Sommerfield condition of no reflection at infinity.

The integral technique can only be applied in cases where the properties of the medium are constant or the differential equation describing the medium can be transformed into a constant property problem. Consequently, the interface separating regions I and II in Fig. 3 must be extended sufficiently far from the exit so that the flow is approximately uniform. In this case, the wave Eq. (4) reduces to

$$F(\phi) = \phi_{rr} + \phi_{r/r} + [1 - M_o^2]\phi_{zz} + \left(k^2 - \frac{m^2}{r^2}\phi\right) + 2ikM_o\phi_z = 0 \quad (21)$$

where

$$k = w/\bar{c} \quad (22)$$

and

$$M_o = \bar{\phi}_z/\bar{c} \quad (23)$$

Using the transformations employed by Tester (14)

$$r^* = r,\ z^* = z\Big/\sqrt{1 - M_o^2},\ k^* = k\Big/\sqrt{1 - M_o^2}$$

$$\phi^* = \phi \exp\left(ikMz^*\Big/\sqrt{1 - M_o^2}\right) \quad (24)$$

Eq. (21) becomes

$$\phi^*_{r^*r^*} + \phi^*_{r^*/r^*} + \phi^*_{z^*z^*} + \left(k^{*2} - \frac{m^2}{r^{*2}}\right)\phi^* = 0 \quad (25)$$

In Ref. (6), Meyer et al. have transformed Eq. (25) along with the appropriate boundary conditions into the integral form. The Meyer et al. approach was used here since their computer codes were made available and the accuracy of the codes has been previously demonstrated.

Iteration Scheme

As mentioned earlier, at the interface between the interior and exterior regions, the initial impedance condition, Eq. (15), is only an approximation. To determine the exact value of the exit impedance as well as the acoustic velocities and pressures, a simple iterative procedure based on the method of successive substitution is formulated as follows:

1. Employ the exit impedance condition ($Z_{1i} = 1.$) and use the finite element method to obtain a solution within the interior region. From this solution compute the acoustic potential $\phi(s)$ at the interface.
2. Let the acoustic potential at the interface as computed in Step 1 equal $g(s)$. Use the integral technique to compute the exterior field. From the exterior solution, compute the impedance at the interface (i.e., Z_{1e}) where the subscript e denotes the external impedance at the interface.
3. If Z_{1e} is not equal to Z_{1i}, set Z_{2i} equal to Z_{1e}, and repeat the solution of the interior region using the finite element method and obtain a new acoustic potential $\phi(s)$ at the interface.
4. Repeat Steps (2) and (3) until Z_{1i} and Z_{1e} agree within a specified tolerance.

DISCUSSION OF RESULTS

As previously outlined, the finite element-integral program is now applied to the JT15D engine configuration for the $m = 13$ mode to determine the far field radiation pattern, suppressor effectiveness, and effect of flight Mach number. Each of these topics will now be considered in order.

For the calculations reported in this paper, the finite element computer code subdivided the interior region into 320 Hermitian elements. These elements use 1003 nodal points of which 683 are triangle vertices with 2049 degrees of freedom (ϕ, ϕ_r, ϕ_z unknowns) and 320 centroid unknowns for a total of 2369 unknowns. The computer code for the integral technique subdivided the interface into 59 segments.

Far Field Radiation Pattern

The calculated far field radiation pattern for the (13,0) mode at 3150 Hz is shown in Fig. 5 at 24.4 m and 5.42 m. The similarity between the two far field distributions indicates that near field effects are absent. The jump at 30° is not real and results from insufficient elements. Fewer elements produce a larger jump. These results are replotted in Fig. 6 along with the experimental data from Ref. (7), for which the single $m = 13$ mode dominates the noise source. The data, presented in graphical form in Ref. (7), are tabulated here in Tables I and II for convenience. For the noise source at the fan plane, both the radial pressure distribution of the (13,0) mode and also a uniform radial pressure distribution in the annulus were used. Since only the (13,0) mode propagates, the far field pressure distribution was identical for both source inputs. This, of course, will not be the case when more than one spinning mode can propagate. As seen in Fig. 6, the analysis and experiment agree reasonably well. The peaks, however, are about 10 degrees apart.

Also shown in Fig. 6 is the far field distribution for a sharp edged inlet based on Savkar's (15) Wiener-Hopf analytical solution. Savkar's theory was modified for convection effects using a velocity correction factor from Ref. (16) (Eq. (8)). As seen in Fig. 6, the sharp lip solution predicts slightly more radiation to the higher angles than the thick bellmouth finite element solution.

Soft Wall Ducts

As mentioned earlier, soft wall suppressors were run in the JT15D inlet to attenuate the sound in the far field. The axial position of the suppressor is shown in Fig. 2. In the experiment only half of the suppressor was active. As seen by the slanted lines originating at nodes 18 and 44 in Fig. 4, the finite element nodes were positioned exactly at the entrance and exit of the active liner. The second half of the suppressor was taped to give a hard wall. With the full suppressor open, the tone level fell below the broadband noise level which prevented a quantitative evaluation of the suppressor's performance. Three suppressor designs were built having estimated nominal values of resistance of 2.272, 1.136, and 0.638 (Table 1, (7)). The suppressors were all specially built to have identical reactances of 0.5 which is stiffness controlled at 3150 Hz.

Figure 7 displays the calculated far field radiation pattern for the same source as in Fig. 5 but with a soft wall suppressor having a resistance of 0.638 and reactance of 0.5. A comparison of Fig. 5 with Fig. 7 shows the sound has the same far field shape but is decreased in magnitude by about 22 dB.

A comparison with the experimental data will now be made with data between 50 and 80 degrees. These angles were chosen since in the experiment the sound pressure level for these angles stood well above the broadband noise floor. At 60 degrees, subtracting the SPL of 69.02 in Fig. 7 from the hard wall value of 91.23 in Fig. 5 yields a calculated attenuation of 22.21 dB. The other angles also have the same theoretical

attenuation. This attenuation along with other calculated attenuations for the other resistance values are plotted in Fig. 8. As seen in Fig. 8, the xperiment and theory are again in reasonable agreement.

Also shown in Fig. 8 is the attenuation calculated using a semi-infinite soft wall duct theory (solid circular point) which considers only the lowest radial mode for m = 13. The maximum attenuation for the semi-infinite duct analysis is 30 dB ((7), pg. 8 or Fig. 9) which is approximately 6 dB higher than the peak numerical prediction and about 13 dB higher than the numerical prediction at $\theta = 1.14$.

Note also that the numerically determined maximum attenuation (at $x = 0.5$) occurs at a lower resistance (~ 0.5) than that determined using a single radial mode ($\theta \sim 1.14$). This difference can be explained using the argument presented in Ref. (7) that modal scattering is important for this extreme case of a single source mode entering a very short acoustic liner (L/D = 0.15). The impedance discontinuity causes the single hardwall mode to scatter into several radial modes in the soft wall section. Since the liner is so short the higher radial modes contribute significantly to the overall suppression. It was shown in Ref. (17) that higher radial modes have progressively lower optimum resistance. It would thus be expected that a multimodal liner solution (which the numerical solution is) would produce a lower optimum resistance than the lowest radial mode solution used to design these liners. This explanation of modal scattering being significant is reinforced by the calculations shown in Fig. 9. As the acoustic liner is lengthened (smaller D/L), the numerically calculated attenuation approaches the single mode attenuation shown at D/L = 0. For an extremely long duct this lowest mode would dominate the sound attenuation.

Flight Mach Number

As mentioned in the introduction, static experiments on test stands as shown in Fig. 10(a) cannot simulate the true flight situation as shown in Fig. 10(b). Although a bellmouth inlet is not a realistic inlet to fly, a calculation will now be performed to demonstrate the capability of the program. Figure 11 shows the far field radiation pattern for the case of flight at 44.7 m/sec (100 miles/hr). A comparison to the static case of Fig. 5 is shown in Fig. 12. As seen in Fig. 12, the noise is shifted by flight to lower angles although the peak did not seem to move. These results cannot be generalized to flight, because a bellmouth inlet would not be used in flight.

LIMITATIONS OF THEORY

As seen in the previous section, the theory is versatile and gives reasonable predictions of the far field radiation pattern and suppressor attenuation. This data was for a nearly cutoff mode with a relatively long wave length. For well propagating modes with relatively short axial wavelength, however, the present computer does not have the storage capacity to resolve the many axial wavelengths. This is particularly true when the Mach approaches unity and the convective effects further shorten the sound wavelength. Therefore, research is continuing (2) using special numerical techniques such as the wave envelope concept (18 and 19) to reduce the required computer storage and the transient technique (20) to completely eliminate matrix storage requirements.

Finally, for well propagating modes the boundary layer can have significant effects (17). The present potential flow formulation does not include the effects of a boundary layer. In this situation, the complete solution to the separate linearized continuity, momentum, and energy equations will be required. With this increased number of unknowns, the wave envelope technique or a transient approach (21 and 22) looks very attractive.

CONCLUSIONS

Finite element theory coupled with the integral technique is a versatile tool for handling noise propagation in engine inlets and radiation to the far field. The theory can also be applied to any situation where the axial wavelength of sound is relatively large, such as an inlet with low frequency sound excitation and low Mach number and an exhause duct where convective effects tend to increase the sound wavelength.

For the single mode JT15D data, the theory and experiment are in reasonably good agreement for the far field pattern as well as the suppressor attenuation. Flight effects are also easily handled by the program.

REFERENCES

1. Baumeister, K. J., Numerical Techniques in Linear Duct Acoustica - A Status Report," Journal of Engineering for Industry, Vol. 103, August 1981, pp. 270-281.
2. Baumeister, K. J., "Numerical Techniques in Linear Duct Acoustics, 1980-1981 Update," NASA TM-82730, 1981.
3. Horowitz, S. J., Sigman, R. K., and Zinn, B. T., "An Iterative Finite Element - Integral Technique for Predicting Sound Radiation from Turbofan Inlets in Steady Flight," AIAA Paper 82-0124, Jan. 1982.
4. Baumeister, K. J., and Majjigi, R. K., "Application of Velocity Potential Function to Acoustic Duct Propagation Using Finite Elements," AIAA Journal, Vol. 18, No. 5, May 1980, pp. 509-514.
5. Bayliss, A., Gunzburger, M., and Turkel, E., "Boundary Conditions for the Numerical Solution of Elliptic Equations in Exterior Regions," NASA CR-153185, 1980.
6. Meyer, W. L., Bell, W. A., Stallybrass, M. P., and Zinn, B. T., "Prediction of the Sound Field Radiated from Axisymmetric Surfaces," Journal of the Acoustical Society of America, Vol. 65, No. 3, Mar. 1979, pp. 631-638.
7. Heidelberg, L. J., Rice, E. J., and Homyak, L., "Acoustic Performance of Inlet Suppressors on an Engine Generating a Single Mode," AIAA Paper 81-1965, 1981.
8. Pai, S. I., Introduction to the Theory of Compressible Flow, Van Nostrand Company, New York, 1959.
9. Majjigi, R. K., "Application of Finite Element Techniques in Predicting the Acoustic Properties of Turbofan Inlets," Ph.D. Thesis, Georgia Inst. of Tech., Atlanta, 1979.
10. Huebner, K. H., The Finite Element Method for Engineers, John Wiley and Sons, Inc., New York, 1975.
11. Sigman, R. K., Majjigi, R. K., and Zinn, B. T., "Determination of Turbofan Inlet Acoustics Using Finite Elements," AIAA Journal, Vol. 16, No. 11, Nov. 1978, pp. 1139-1145.
12. Astley, R. J., Walkington, N. J., and Eversman, W., "Accuracy and Stability of Finite Element Schemes for the Duct Transmission Problem," AIAA Paper 81-2015, Oct. 1981.

13. Conte, S. P., and de Boor, C., Elementary Numerical Analysis, 2nd ed., McGraw-Hill Book Company, Inc., New York, 1971.
14. Tester, B. J., "The Propagation and Attenuation of Sound in Lined Ducts Containing Uniform or 'Plug' Flow," Journal of Sound and Vibration, Vol. 28, No. 2, May 1973, pp. 151-203.
15. Savkar, S. D., "Radiation of Cylindrical Duct Acoustic Modes with Flow Mismatch," Journal of Sound and Vibration, Vol. 42, No. 3, Oct. 1975, pp. 363-386.
16. Heidmann, M. F., Saule, A. V., and McArdle, J. G., "Predicted and Observed Modal Radiation Patterns from JT15D Engine with Inlet Rods," Journal of Aircraft, Vol. 17, No. 7, July 1980, pp. 493-499.
17. Rice, E. J., "Optimum Wall Impedance for Spinning Modes - A Correlation with Mode Cut-Off Ratio," Journal of Aircraft, Vol. 16, No. 5, May 1979, pp. 336-386.
18. Baumeister, K. J., "Wave Envelope Analysis of Sound Propagation in Ducts with Variable Axial Impedance," Aeroacoustics: Fan Noise and Control: Duct Acoustic; Rotor Noise, I. R. Schwartz, H. T. Nagamatsu, and W. Strahle, eds., Progress in Astronautics and Aeronautics Series, Vol. 44, American Institute of Aeronautics and Astronautics, New York, 1976, pp. 451-474.
19. Astley, R. J., and Eversman, W., "A Note on the Utility of a Wave Envelope Approach in Finite Element Duct Transmission Studies," Journal of Sound and Vibration, Vol. 76, No. 4, June 1981, pp. 595-601.
20. White, J. W., "A General Mapping Procedure for Variable Area Duct Acoustics," AIAA Paper 81-0094, Jan. 1981.
21. Baumeister, K. J., "Time Dependent Difference Theory for Noise Propagation in a Two-Dimensional Duct," AIAA Journal, Vol. 18, No. 12, Dec. 1980, pp. 1470-1476.
22. Baumeister, K. J., "A Time Dependent Difference for Sound Propagation in Ducts witn Flow," Presented at 98th Meeting of the Acoustical Society of America, Salt Lake City, Utah, Nov. 1979.

TABLE I

HARD WALL JT15D TEST INLET - Fig. 6
(Far field 24.38 m, 3150 Hz, m = 13, Ref. (7))

	SPL Angle from inlet, degrees					
	40	50	60	70	80	90
Run 1	88.5	94.0	95.6	95.4	90.0	85.5
Run 2	87.2	94.4	96.4	96.0	90.5	87.7
Run 3	88.5	96.3	96.0	95.7	89.5	84.6
Run 4	88.1	96.2	97.7	96.3	90.2	85.0
Run 5	88.8	96.7	97.8	96.1	90.0	86.4
Run 6	88.5	96.3	96.7	95.2	90.3	85.7
Average	88.3	95.7	96.7	95.8	90.1	85.8
Normalized	91.6	99.0	100.0	99.1	93.4	89.1

TABLE II

FAR FIELD SOFT WALL JT15D SPL ATTENUATION - Fig. 8
(χ = 0.5, Ref. (7))

Wall Resistance	Runs	SPL Angle from inlet, degrees			
		50	60	70	80
2.272	Run 1	8.5	9.6	9.6	9.0
	Run 2	7.4	8.8	10.7	10.0
	Average	8.0	9.2	10.2	9.5
1.136	Run 3	19.2	17.6	20.7	18.3
	Run 4	16.2	17.9	20.3	20.8
	Average	17.7	17.8	20.5	19.6
0.638	Run 5	23.7	24.0	21.6	19.0
	Run 6	22.2	20.6	20.0	20.5
	Average	23.0	22.3	20.8	19.8

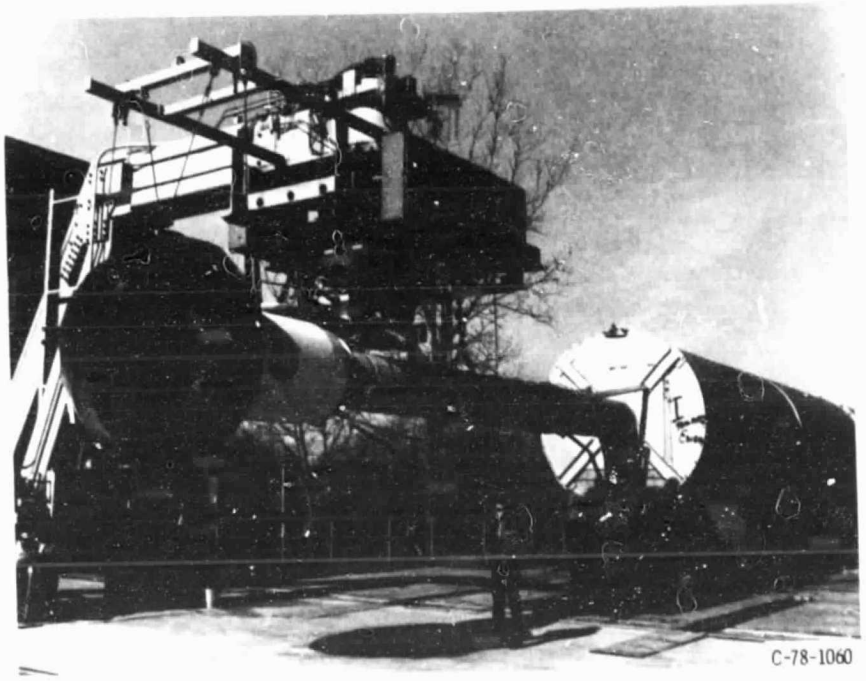

Figure 1. - JT15D engine with inflow control device on test stand with exhaust muffler.

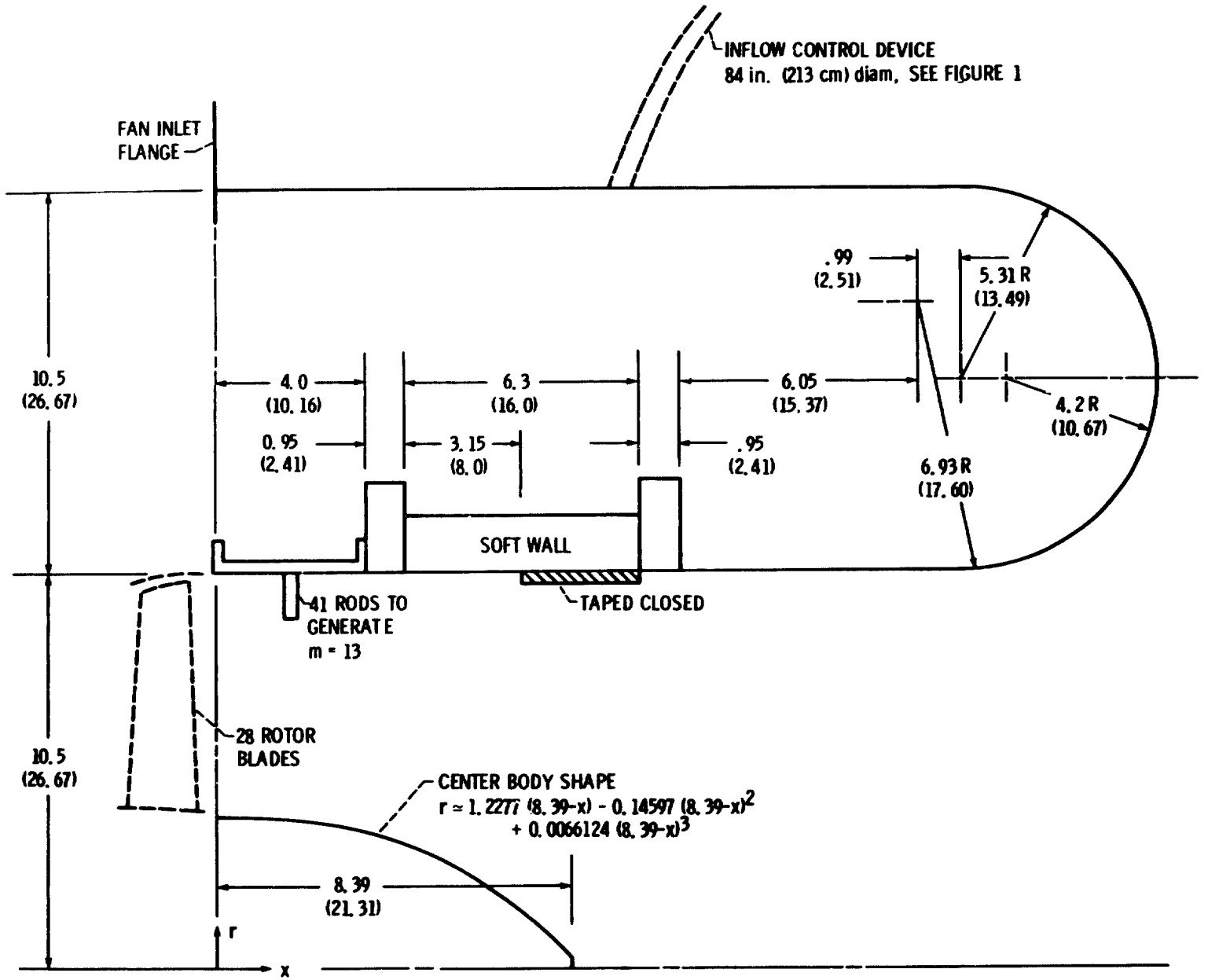

Figure 2. - Test configuration of JT15D engine inlet used for single mode SDOF suppressor experiments, dimensions in inches (cm).

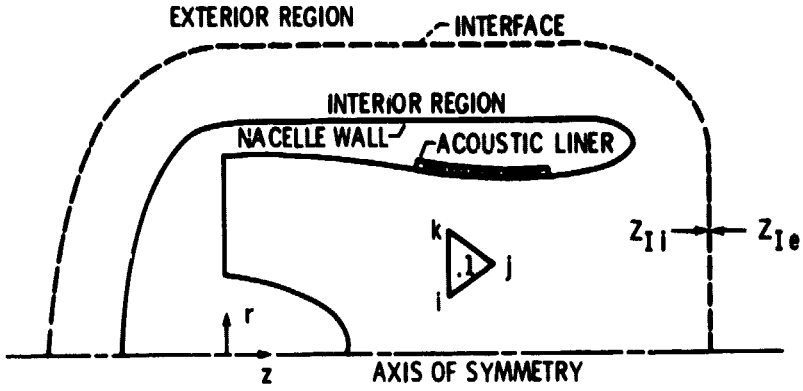

Figure 3. - Geometry of an idealized inlet.

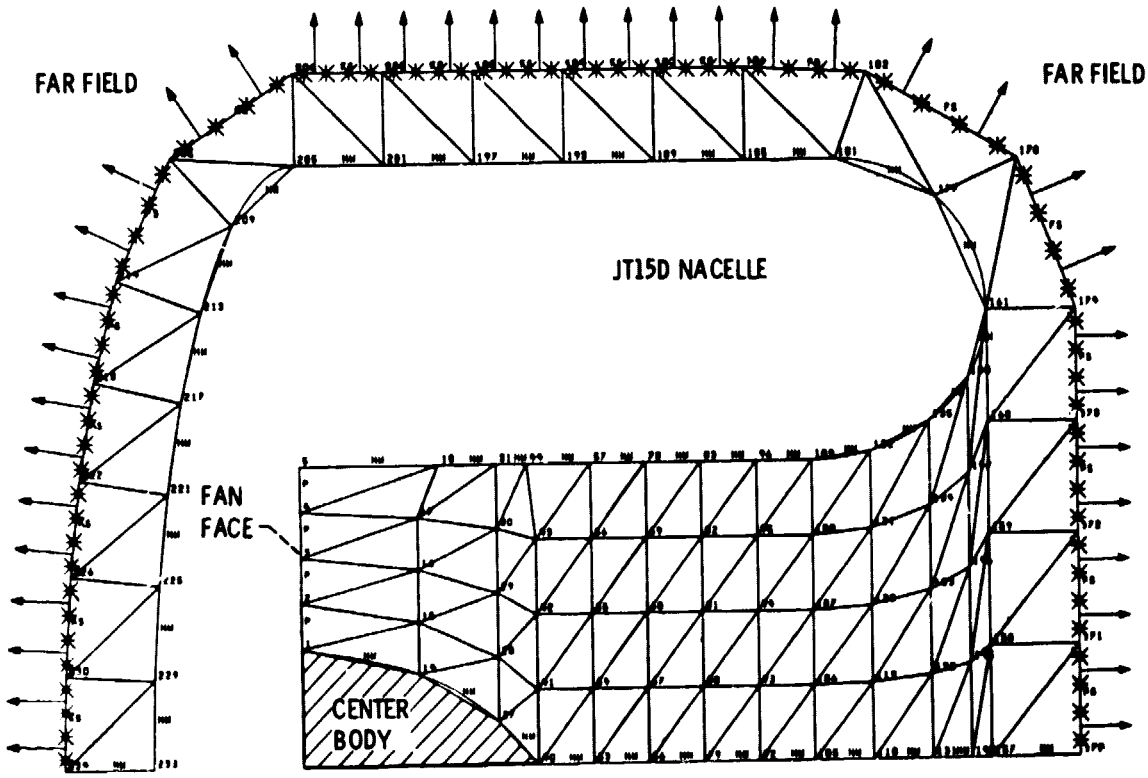

Figure 4. - Division of JT15D inlet into Hermitian triangular elements.

ANGLE, deg	SPL, dB R = 20kr$_0$	SPL, dB R = 90kr$_0$
0.00	-.81	-13.51
10	15.07	4.57
20	61.49	49.83
30	81.31	65.70
40	99.44	85.80
50	105.87	92.66
60	104.29	91.23
70	101.31	87.86
80	97.77	84.75
90	93.17	80.40

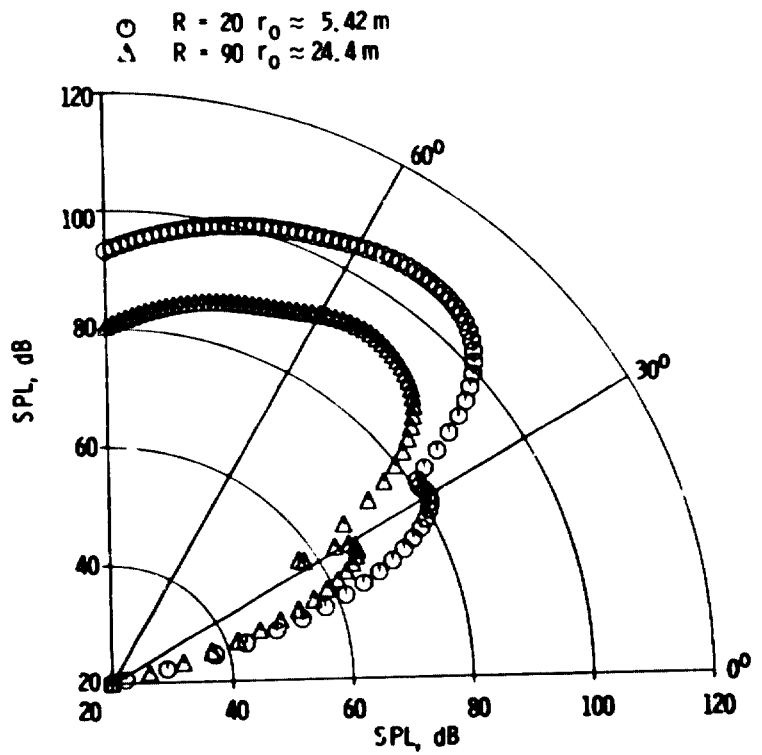

Figure 5. - Theoretical far field SPL directionality pattern for 3150 Hz and (13, 0) mode at source for hard wall configuration.

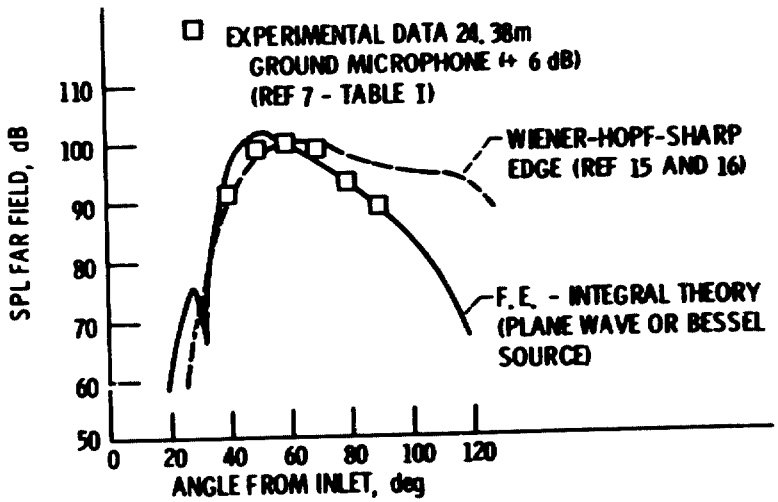

Figure 6. - Comparison of theory and experiment for narrow band tone directivity pattern at 3150 Hz and (13, 0) mode for hard wall configuration (theory and data normalized to 100 dB at 60 deg).

ANGLE, deg	SPL, dB $R = 20xr_0$	SPL, dB $R = 90xr_0$
00.00	-22.99	-35.82
10	-7.12	-17.63
20	39.29	27.62
30	59.07	43.46
40	77.22	63.58
50	83.66	70.45
60	82.07	69.02
70	79.10	65.65
80	75.56	62.54
90	70.96	58.19

○ $R = 20\ r_0 \approx 5.42$ m
△ $R = 90\ r_0 \approx 24.4$ m

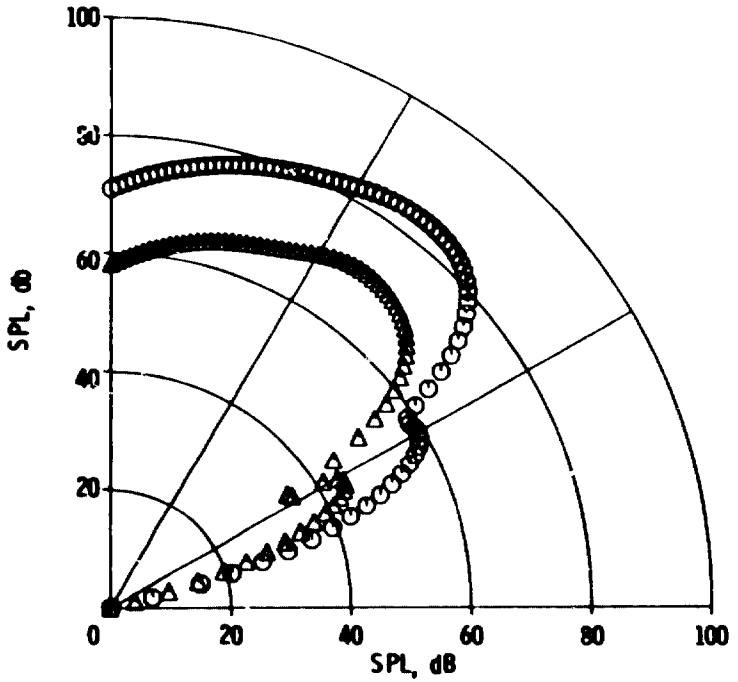

Figure 7. - Theoretical far field SPL directionality pattern for 3150 Hz and (13, 0) mode at source for soft wall configuration ($\Theta = 0.638$, $\chi = 0.5$) with plane wave input.

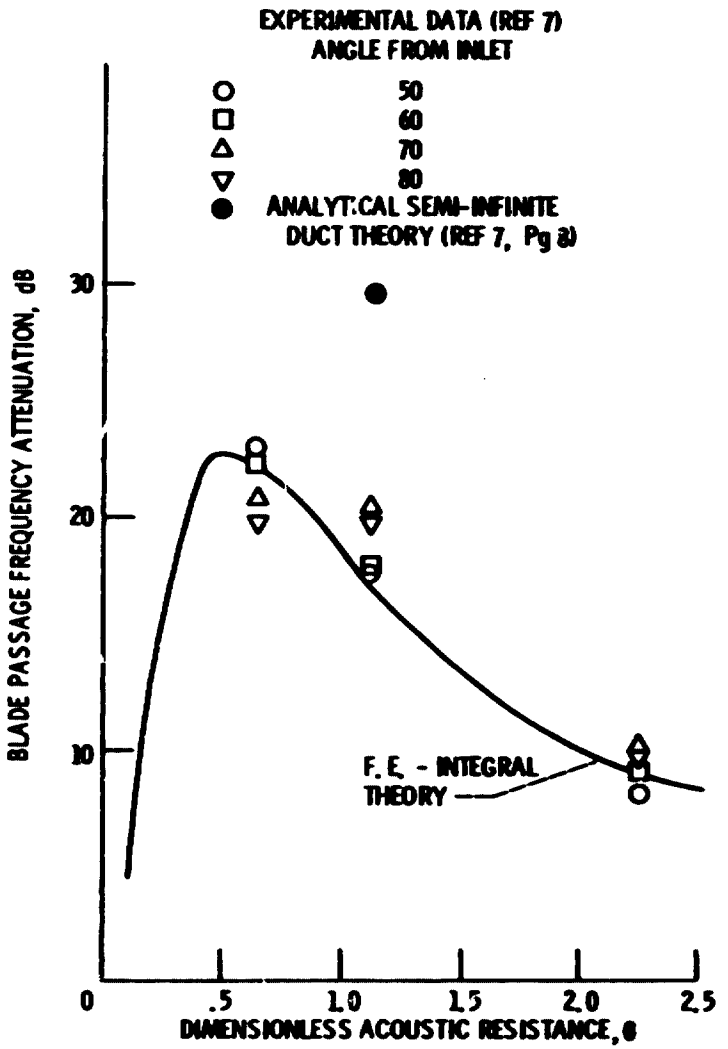

Figure 8. - Comparison of data with theoretical attenuation as a function of resistance for the (13, 0) mode at 3150 Hz (reactance $\chi = 0.5$) between 50-80 deg from inlet center line.

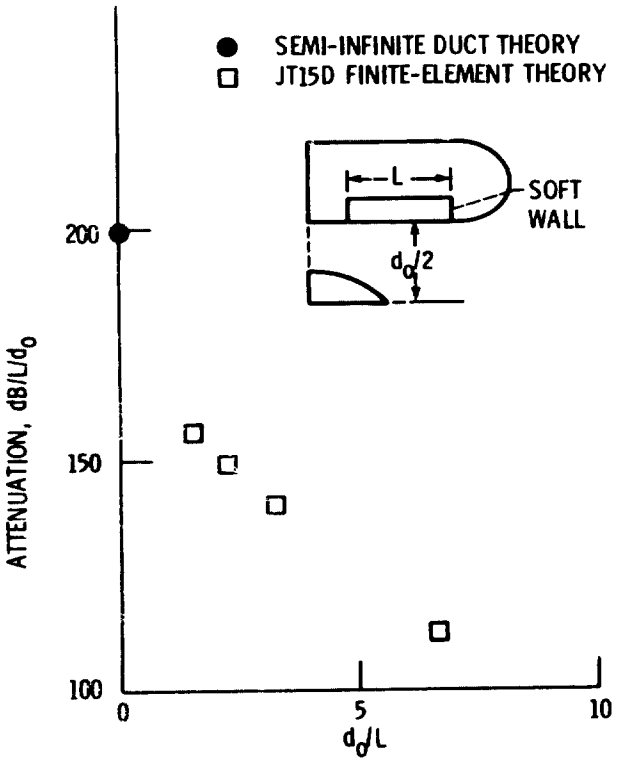

Figure 9. - Effect of liner length on normalized total liner attenuation for $\theta = 1.136$ and $\chi = 0.5$.

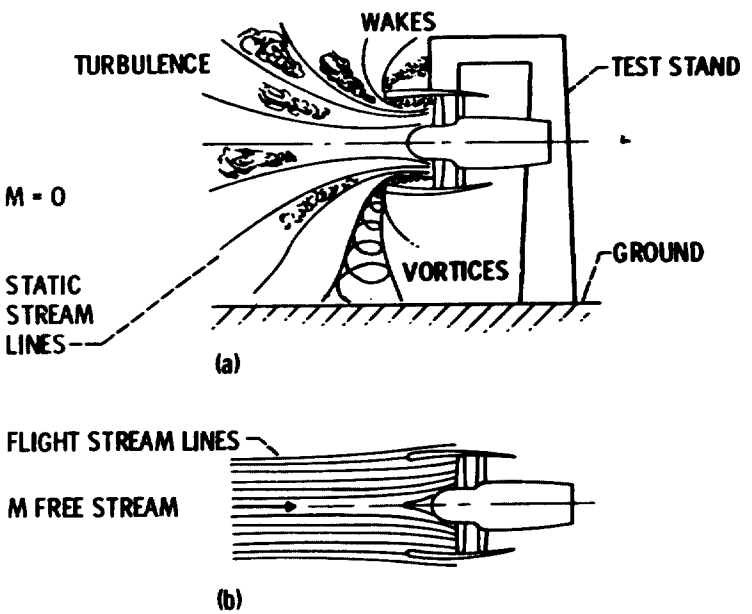

(a) Static test.

(b) Flight test.

Figure 10. - Effect of forward velocity on inlet stream lines.

ANGLE, deg	SPL, dB R = 20xr_0	SPL, dB R = 90xr_0
00.00	-1.90	-13.34
10	13.34	5.19
20	69.54	55.85
30	94.29	81.26
40	103.24	90.13
50	108.66	95.34
60	106.39	93.35
70	101.02	87.79
80	95.03	82.06
90	88.21	75.59

○ R = 20 r_0 ≈ 5.42m
△ R = 90 r_0 ≈ 24.4m

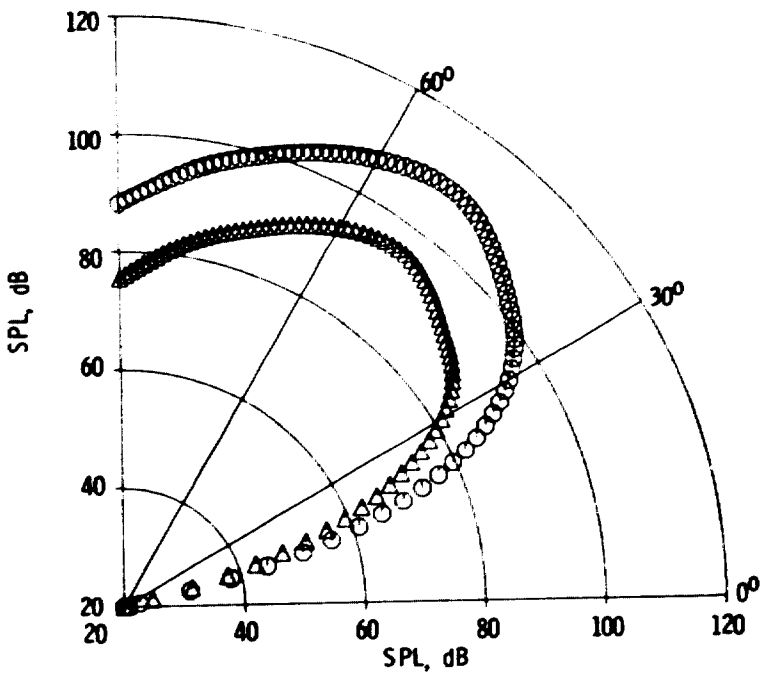

Figure 11. - Theoretical far field SPL directionality pattern for flight at 44.7 m/sec (100 miles/hr) for 3150 Hz and (13, 0) plane mode at source for hard wall configuration.

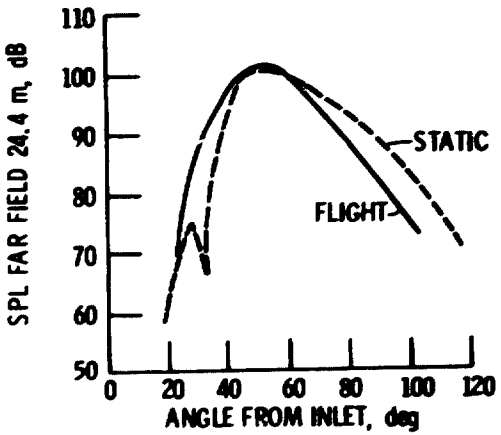

Figure 12. - Comparison of the calculated far field SPL level with flight at 44.7 m/s (100 mi/hr) for narrow band tone directivity pattern at 3150 Hz and (13, 0) mode for hard wall configuration.